

Dielectric Loaded Waveguide Terahertz LINACs

Mostafa Vahdani,^{1,2,*} Moein Fakhari,¹ and Franz X. Kärtner^{1,2,3}

¹*Center for Free-Electron Laser Science CFEL,*

Deutsches Elektronen-Synchrotron DESY, Notkestrasse 85, 22607 Hamburg, Germany

²*Department of Physics, Universität Hamburg, Jungiusstrasse 9, 20355 Hamburg, Germany*

³*The Hamburg Center for Ultrafast Imaging, Luruper Chaussee 149, 22761 Hamburg, Germany*

Dielectric loaded waveguides (DLWs) driven by multicycle terahertz (THz) pulses hold great promise as compact linear accelerators (LINACs) due to their ability to sustain higher breakdown fields at THz frequencies compared to conventional RF components. Precise control of the THz pulse's phase and group velocities within the DLW can be achieved by adjusting the dimensions of the dielectric tube. Optimization of the DLW parameters has to take various factors into account like initial electron energy, THz pulse energy available, THz pulse width, DLW dimensions, etc. To maximize the final kinetic energy of the accelerated electrons, this study presents a comprehensive analytical/numerical guideline for cylindrical DLW LINACs. Additionally, graphic representations are introduced to visualize optimal designs for varying initial electron and THz pulse energies. The provided guideline figures enable designers to tailor the accelerator to specific requirements, paving the way for potential advancements in THz-driven particle acceleration and offering cost-effective alternatives to conventional RF accelerators for various scientific, industrial, and medical applications.

I. INTRODUCTION

Conventional Radio Frequency (RF) accelerators operate by using alternating electric fields to accelerate charged particles, such as electrons, to high energies. A higher acceleration gradient is always preferable and will result in an increase in bunch quality since space charge affects the beam, especially as long as the beam is sub-relativistic. In order to increase the acceleration gradient, one needs to increase the accelerating electric field which is limited by field-emission at metal surfaces (breakdown voltage) in conventional RF accelerators. It was always a dream for accelerator physicists to go to higher operating frequencies because of the expected higher breakdown fields [1–3]. Laser driven accelerators such as Dielectric Laser Accelerators (DLA) can achieve GV/m accelerating fields. However, the short wavelength of the fields and small cross sectional area of the accelerator significantly limits the bunch charge [4–6]. Extremely high timing precision is also required for injecting electron bunches due to short wavelength of optical fields. The short wavelength also results in an increased energy spread and emittance growth. Other methods such as plasma-based acceleration were developed to overcome these limitations [7–11]. Plasma waves can be produced by intense laser pulses or high charge electron bunches in plasmas. Laser Plasma Accelerators (LPA) suffer however from plasma instabilities and as recently shown need exquisite control on the drive laser pulses to achieve high energy stability and good beam quality [12–14]. This is where Terahertz (THz) frequencies come into play, offering a potential solution to mitigate these limitations, since the accelerating structure is still a solid state device [15–19]. Another advantage of THz frequencies lies

in their ability to allow for higher field gradients due to the shorter pulse duration available at higher frequencies and the shorter wavelength when compared to RF-waves. Still significant charge can be accelerated with excellent beam quality, stability and most importantly lower emittance or higher brightness due to the increased field strength, making them an attractive candidate for particle accelerators. Break down fields at THz frequencies, e.g. 100-300 GHz can be considerably higher when compared to the RF at 3 GHz using the scaling rules empirically confirmed [20–22]. Also, THz sources both in the single-cycle and multi-cycle regime are becoming increasingly mature [23], but are yet by far not as high developed as RF-sources.

The advancements in THz-driven accelerators can potentially lead to more compact and cost-effective acceleration systems, offering an alternative to conventional RF accelerators and enabling new scientific discoveries, industrial applications, and medical treatments that rely on high-energy particle beams. In recent years THz-driven accelerators have emerged as a promising field of research, driven by advancements in THz source technologies. Many groups are actively exploring various methods and techniques to harness the potential of THz-driven accelerators and beam manipulation devices.

THz accelerators driven by single-cycle THz pulses generated through nonlinear crystals have been studied and developed over the past decade [18, 24]. While multi-cycle THz accelerators employing resonant cavities have shown promise for accelerator device implementation [25], challenges still persist in fabricating metallic structures with the required surface quality at THz frequencies. Traveling wave linear accelerators present another type of particle accelerator in the THz spectrum and have long been considered a viable solution. The idea of using traveling waves for electron acceleration has been already explored for RF accelerators [26]. The phase ve-

* mostafa.vahdani@desy.de

locity of the traveling wave in the accelerator waveguide must be reduced to match the electron bunch velocity for optimal interaction between electrons and the electromagnetic wave, facilitating efficient acceleration. This reduction is typically achieved through the utilization of slow wave structures like corrugated waveguides or Dielectric Loaded Waveguides (DLW). THz traveling wave can be generated either externally, for example, by nonlinear crystals or internally via a colinear intense driving beam using Cerenkov radiation (wake fields) [27–29]. It is noted that in the configuration of two-beam accelerators (TBA), a modified version of colinear wakefield accelerators, the generated electromagnetic wave is transferred to a separate waveguide hosting the main beam (witness beam) [30, 31].

DLWs have emerged as a particularly attractive option for multicycle THz acceleration, primarily due to their ease of fabrication. While the concept of employing DLWs for RF accelerators dates back to 1947 [32, 33], their practicality and favorability have become more pronounced in the THz regime. During the last decade, many studies have focused on implementing THz accelerators using DLWs in both rectangular [34] and cylindrical structures [15, 35–37]. Cylindrical DLWs, in particular, offer superior field uniformity compared to their rectangular counterparts (will be discussed in this paper). In addition, it has been shown, that DLWs in conjunction with metallic wire waveguides and surface waves enables the efficient implementation of THz accelerators [38, 39].

In this paper our focus is on optimizing the structure of cylindrical DLWs for THz acceleration. The design of cylindrical DLW LINACs involves incorporating a dielectric layer to reduce the phase velocity, as the metallic waveguides exhibit phase velocities exceeding the speed of light. Furthermore, the addition of a dielectric layer unavoidably reduces the group velocity, limiting the interaction length between the electrons and the accelerating field within the DLW. In this context, multi-cycle THz pulses are used for increasing the interaction length, as they provide more cycles with lower bandwidth, thereby reducing the dispersion effect within the waveguide. In the simulations conducted, a rectangular THz pulse along the DLW is considered. If the pulse is sufficiently long and narrow-band, it is possible to neglect the dispersion effect of the waveguide. However, the envelope velocity of the pulse within the waveguide is still calculated and taken into account to ensure more accurate modeling and analysis. In the first section of this paper, we explore the electromagnetic characteristics of the DLW. Subsequently, in the second section, we focus on optimizing the DLW dimensions and THz pulse properties to maximize energy gain. We also present the key parameters that need to be initialized, varied, or optimized. Finally, in the third section, we briefly discuss the effects of the DLW LINAC on axial parameters of an electron bunch.

II. ELECTROMAGNETIC FIELD COMPUTATION

Here, we employ an analytical/numerical approach to investigate the electromagnetic fields in a cylindrical DLW LINAC which is depicted schematically in Fig. 1. The metallic layer has to be thick compared to the skin depth of the metal to effectively confine the fields within the structure.

For the DLW design and optimization of electron acceleration along the DLW, the exact solutions for the electromagnetic fields within the tube need to be found. Typically, the coupling between the electron beam current and the electromagnetic wave complicates the analysis. However, in the THz regime, where low charge single bunches are assumed, the influence of the beam current on the electromagnetic wave becomes negligible, allowing for decoupling of the two phenomena. Consequently, the problem becomes easier to solve using numerical and analytical methods.

Solving Maxwell’s equations along with applying the boundary conditions and continuity of the electric and magnetic fields in the waveguide results in the waveguide modes. Field distributions with vanishing longitudinal electric field component are called Transverse Electric (*TE*) modes and those with vanishing longitudinal magnetic field are Transverse Magnetic (*TM*) modes. The DLW structure depicted in Fig. 1 also supports Hybrid Electromagnetic Modes (*HEM*) due to having two media with different refractive indices. *HEM* modes have both electric field and magnetic field longitudinal field components.

The cylindrical *TM*₀₁ mode (we will explore the indices in the following section) is identified as the optimal mode for particle acceleration due to its strong longitudinal electric field along the axis for a given input power. The subsequent section presents a rigorous determination of the field distribution for this mode.

A. Field distribution

From electromagnetic field theory we know that the electric and magnetic fields in a homogeneous source free region can be expressed in terms of the vector potential \vec{A} as [40]

$$\vec{E} = -j\omega\mu\vec{A} + \frac{1}{j\omega\epsilon}\nabla(\nabla\cdot\vec{A}) \quad (1a)$$

$$\vec{H} = \nabla\times\vec{A} \quad (1b)$$

There is an arbitrariness in the choice of vector potentials. For *TM* modes the magnetic vector potential \vec{A} has only a longitudinal component, Ψ , i.e.

$$\vec{A} = \vec{u}_z\Psi \quad (2)$$

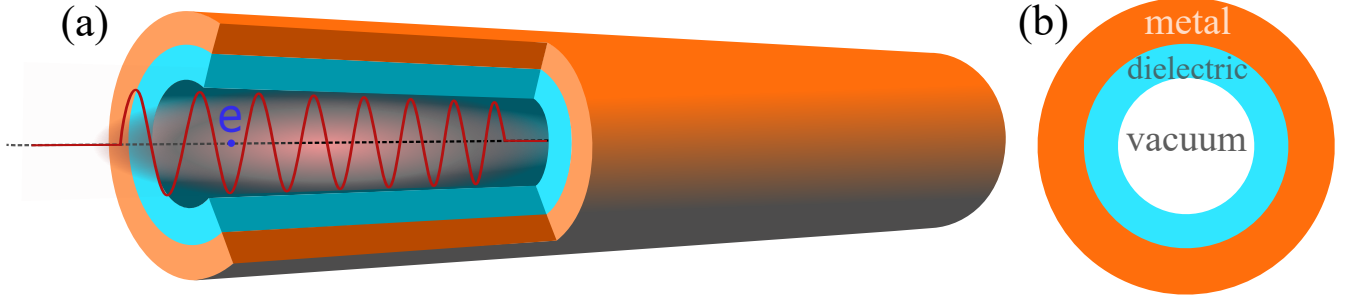


FIG. 1. (a) DLW structure comprising a dielectric tube (light blue) surrounded by a metallic layer (orange) functioning as a THz LINAC (b) cross sectional view of the DLW.

which obeys the scalar Helmholtz equation. Due to the cylindrical symmetry of the DLW structure, we write the Helmholtz equation for Ψ in cylindrical coordinates.

$$\frac{1}{\rho} \frac{\partial}{\partial \rho} \left(\rho \frac{\partial \Psi}{\partial \rho} \right) + \frac{1}{\rho^2} \frac{\partial^2 \Psi}{\partial \phi^2} + \frac{\partial^2 \Psi}{\partial z^2} + k^2 \Psi = 0, \quad k^2 = \omega^2 \mu \epsilon \quad (3)$$

Here, ϵ and μ denote the medium's permittivity and permeability, respectively. By utilizing the method of separation of variables in cylindrical coordinates, the wave functions Ψ can be expressed as the product of functions $R(\rho)$, $\Phi(\phi)$, and $Z(z)$.

$$\Psi = R(\rho) \Phi(\phi) Z(z) \quad (4)$$

Substitution of Ψ into Eq. (3) and division by Ψ will result in

$$\frac{1}{\rho R} \frac{d}{d\rho} \left(\rho \frac{dR}{d\rho} \right) + \frac{1}{\rho^2 \Phi} \frac{d^2 \Phi}{d\phi^2} + \frac{1}{Z} \frac{\partial^2 Z}{\partial z^2} + k^2 = 0 \quad (5)$$

Since the third term is independent of ρ and ϕ , and cannot be a function of z , it must be equal to a constant.

$$\frac{1}{Z} \frac{\partial^2 Z}{\partial z^2} = -k_z^2 \quad (6)$$

substituting Eq. (6) into Eq. (5) and multiplying by ρ^2 yields:

$$\frac{\rho}{R} \frac{d}{d\rho} \left(\rho \frac{dR}{d\rho} \right) + \frac{1}{\Phi} \frac{d^2 \Phi}{d\phi^2} + (k^2 - k_z^2) \rho^2 = 0 \quad (7)$$

The second term is solely a function of ϕ while the rest of terms are functions of ρ . Therefore

$$\frac{1}{\Phi} \frac{d^2 \Phi}{d\phi^2} = -m^2 \quad (8)$$

The constant m must be an integer due to the periodic nature of $\Phi(\phi)$ in cylindrical coordinates. Consequently, the equation for $R(\rho)$ can be transformed into Bessel's equation.

$$\rho \frac{d}{d\rho} \left(\rho \frac{dR}{d\rho} \right) + ((k^2 - k_z^2) \rho^2 - m^2) R = 0. \quad (9)$$

Eqs. (6) and (8) reveal that $\Phi(\phi)$ and $Z(z)$ are solutions of the harmonic equation, resulting in harmonic functions. $R(\rho)$ in Eq. (9) adheres to Bessel's equation of order n and can be represented using Bessel functions of the first kind, $J_m(k_\rho \rho)$, and Bessel functions of the second kind (Neumann function) $Y_m(k_\rho \rho)$ or Hankel functions of the first and second kind $H_m^{(1)}(k_\rho \rho)$ and $H_m^{(2)}(k_\rho \rho)$, respectively. The term $k^2 - k_z^2$ can be replaced by k_ρ^2 which corresponds to the radial component of the wave vector k . Hence, the wave function Ψ in Eq. (4) is expressed in terms of the functions

$$Z(z) \sim e^{-jk_z z}, e^{jk_z z} \quad (10)$$

$$\Phi(\phi) \sim e^{-jm\phi}, e^{jm\phi}, \sin(m\phi), \cos(m\phi) \quad (11)$$

$$R(\rho) \sim J_m(k_\rho \rho), Y_m(k_\rho \rho), H_m^{(1)}(k_\rho \rho), H_m^{(2)}(k_\rho \rho). \quad (12)$$

Now we are able to compute the electric and magnetic fields of TM modes by using Eq. (1) from the magnetic vector potential \vec{A} as follows [40].

$$\begin{aligned} E_\rho &= \frac{1}{j\omega\epsilon} \frac{\partial^2 \Psi}{\partial \rho \partial z} & H_\rho &= \frac{1}{\rho} \frac{\partial \Psi}{\partial \phi} \\ E_\phi &= \frac{1}{j\omega\epsilon\rho} \frac{\partial^2 \Psi}{\partial \phi \partial z} & H_\phi &= -\frac{\partial \Psi}{\partial \rho} \\ E_z &= \frac{1}{j\omega\epsilon} \left(\frac{\partial^2}{\partial z^2} + k^2 \right) \Psi & H_z &= 0 \end{aligned} \quad (13)$$

For the TM modes of concentric cylindrical multilayer structures which exhibit axial symmetry ($\frac{\partial \psi}{\partial \phi} = 0, m = 0$), the electric and magnetic fields of the i -th layer (see Fig. 2) are formulated as:

$$\begin{aligned}
E_z(\rho, z) &= \left[A_i \begin{Bmatrix} J_0(k_{\rho_i}\rho) \\ H_0^{(1)}(k_{\rho_i}\rho) \end{Bmatrix} + B_i \begin{Bmatrix} Y_0(k_{\rho_i}\rho) \\ H_0^{(2)}(k_{\rho_i}\rho) \end{Bmatrix} \right] e^{-jk_z z} & E_\phi(\rho, z) &= 0 \\
E_\rho(\rho, z) &= -\frac{jk_z}{k_{\rho_i}} \left[A_i \begin{Bmatrix} J_1(k_{\rho_i}\rho) \\ H_1^{(1)}(k_{\rho_i}\rho) \end{Bmatrix} + B_i \begin{Bmatrix} Y_1(k_{\rho_i}\rho) \\ H_1^{(2)}(k_{\rho_i}\rho) \end{Bmatrix} \right] e^{-jk_z z} & H_\rho(\rho, z) &= 0 \\
H_\phi(\rho, z) &= -\frac{j\omega\varepsilon_{d_i}}{k_{\rho_i}} \left[A_i \begin{Bmatrix} J_1(k_{\rho_i}\rho) \\ H_1^{(1)}(k_{\rho_i}\rho) \end{Bmatrix} + B_i \begin{Bmatrix} Y_1(k_{\rho_i}\rho) \\ H_1^{(2)}(k_{\rho_i}\rho) \end{Bmatrix} \right] e^{-jk_z z} & H_z(\rho, z) &= 0
\end{aligned} \tag{14}$$

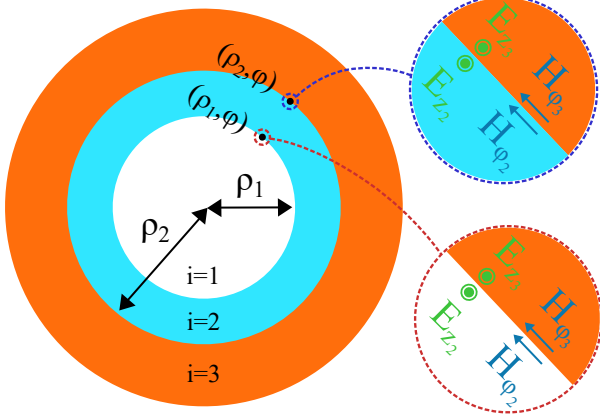


FIG. 2. Tangential electric and magnetic fields of the axial symmetric TM_{0n} -modes at the two interfaces of the DLW with vacuum at radius ρ_1 and the dielectric with the metal at ρ_2 .

where the Hankel functions are used for the outer layer and Bessel and Neumann functions are used for the two inner layers. The coefficient of the Neumann function $Y_0(k_{\rho_1}\rho)$ for the first layer is zero since the Neumann functions have a singularity at the origin. To account for the behavior of the outer layer, only the first kind (or second kind depends on the definition) of Hankel function $H_0^{(1)}(k_{\rho_3}\rho)$ is utilized since the fields need to approach zero as the radius ρ goes to infinity.

In general, k_z can be a complex number when dealing with lossy structures. To establish the relationship among the unknown variables, it is essential to write the continuity equations at the interfaces. Tangential electric and magnetic fields must be continuous functions of ρ at both interfaces for any angle ϕ (Fig. 2).

For a three-layer structure with a vacuum core, expressing the matrix form of the continuity of electric and magnetic fields at both interfaces results in Eq. (15).

$$\begin{bmatrix} J_0(k_{\rho_1}\rho_1) & -J_0(k_{\rho_2}\rho_1) & -Y_0(k_{\rho_2}\rho_1) & 0 \\ \frac{\varepsilon_1 J_1(k_{\rho_1}\rho_1)}{k_{\rho_1}} & -\frac{\varepsilon_2 J_1(k_{\rho_2}\rho_1)}{k_{\rho_2}} & -\frac{\varepsilon_2 Y_1(k_{\rho_2}\rho_1)}{k_{\rho_2}} & 0 \\ 0 & -J_0(k_{\rho_2}\rho_2) & -Y_0(k_{\rho_2}\rho_2) & H_0^{(1)}(k_{\rho_3}\rho_2) \\ 0 & -\frac{\varepsilon_2 J_1(k_{\rho_2}\rho_2)}{k_{\rho_2}} & -\frac{\varepsilon_2 Y_1(k_{\rho_2}\rho_2)}{k_{\rho_2}} & \frac{\varepsilon_3 H_1^{(1)}(k_{\rho_3}\rho_2)}{k_{\rho_3}} \end{bmatrix} \begin{bmatrix} A_1 \\ A_2 \\ B_2 \\ A_3 \end{bmatrix} = \begin{bmatrix} 0 \\ 0 \\ 0 \\ 0 \end{bmatrix} \tag{15}$$

In order to satisfy Eq. (15), the determinant of the coefficient matrix is set to zero (characteristic equation), resulting in nontrivial solutions for the fields. Now the only unknown variable remaining in the characteristic equation is the longitudinal component of the wave vector k_z that can be determined using numerical techniques. Consequently, we can find the electromagnetic field distribution of the TM_{01} -mode in the DLW and important properties such as the phase velocity, group velocity, and attenuation coefficient, providing valuable insights into the behavior of the wave propagation within the structure. It's important to acknowledge that the aim of this paper is to provide a general exploration of DLW design principles. However, to quantitatively demonstrate the influence of various parameters and graphically show the design procedure specific values for some parameters

must be chosen. Table I lists the parameters assumed in solving the characteristic equation of the DLW. Please note that we collectively define and optimize all the parameters in the third section.

Fig. 3 displays contours representing the loci of the zeros of the real and imaginary parts of the determinant (characteristic equation) as a function of the complex values of k_z for the DLW (in order to avoid any singularity caused by k_{ρ_2} which is the denominator of some elements of the coefficient matrix, we multiply the second and fourth rows of the matrix by k_{ρ_2} and calculate the determinant afterwards).

As seen in Fig. 3, Eq. (15) does not have only one solution for k_z , each solution corresponds to one of the TM_{0n} modes. The TM_{01} mode is the first propagating TM mode among the solutions inside the DLW which has

TABLE I. DLW parameters

Parameter	Value
Frequency	300 GHz
DLW dimensions	
Vacuum radius	200 μm
Dielectric thickness	143.1 μm
Material properties	
Conductivity of metal	5.9e7 S/m
Dielectric refractive index	1.95
Dielectric attenuation constant (300 GHz)	~ 10 Np/m

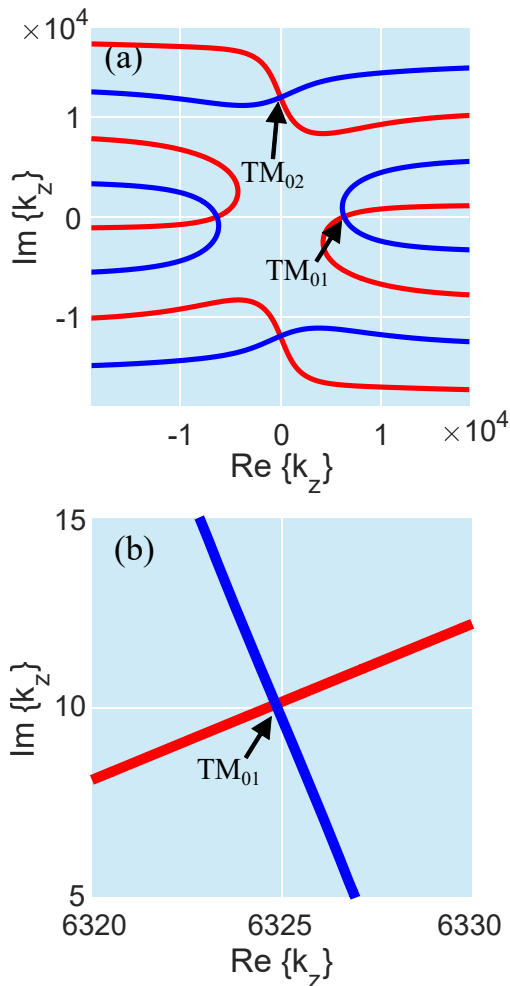


FIG. 3. Loci of the zeros of real and imaginary part of the coefficient matrix determinant in the complex k_z -plane. (b) High resolution graph near one of the complex zeros in the k_z -plane.

the highest real value for k_z .

Subsequently, the electric field distribution is calculated using Eq. (14) for the TM_{01} -mode within the DLW and it is illustrated in Fig. 4.

As depicted in Fig. 4, the z -component of the electric field E_z exhibits complete uniformity across the entire

vacuum aperture ($k_{\rho 1} = k_0^2 - k_z^2 \cong 0$) whenever the phase velocity is set to the speed of light ($\frac{\omega}{\text{Re}\{k_z\}} = \frac{\omega}{k_0}$). Notably, in case of a lossy structure ($\text{Im}\{k_z\} \neq 0$), $k_{\rho 1}$ does not vanish anymore resulting in a small nonuniformity of E_z . However, since the attenuation level is not high here ($\text{Re}\{k_z\} \gg \text{Im}\{k_z\}$), the $k_{\rho 1}$ value is sufficiently low and does not change the uniformity of E_z in the vacuum area considerably. With these assumptions, the terms $\frac{J_1(k_{\rho 1}\rho)}{k_{\rho 1}}$ and $J_0(k_{\rho 1}\rho)$ in Eq. (14) approach $\frac{\rho}{2}$ and 1, respectively, resulting in a simple relation between the field components. As a consequence, the radial and axial (longitudinal) electric fields in the vacuum region are related by

$$\frac{E_\rho}{E_z} \cong -\frac{j\pi\rho}{\lambda} \quad (16)$$

as the phase velocity equals to the speed of light. As inferred from Eq. (16) the radial and longitudinal components of the electric field are $\frac{\pi}{2}$ out of phase. At the peak acceleration phase, as shown in Fig. 4(b), the radial electric field is nearly zero and gradually increases over time and is always a linear function of ρ . As a consequence of Eq. (16), the radial electric field component rises to approximately 63% of the maximum longitudinal electric field magnitude after one-quarter of a period at the dielectric interface for a DLW with 200 μm vacuum radius at 300 GHz operating frequency (Fig. 4(d)). The angular component of the magnetic field can also be expressed with the help of radial component of electric field by Eq. (14) ($H_\phi = \frac{\omega\varepsilon_{d_i}}{k_z} E_\rho$). Given that the imaginary part of the term $\frac{\varepsilon_{d_i}}{k_z}$ is negligible compared to its real part, H_ϕ is an in-phase linear function of E_ρ . This implies that when the electron experiences the peak acceleration field (Fig. 4(b)) the magnetic field does not affect the electron's motion. But as the electron approaches phases with zero longitudinal electric field, the force due to the magnetic field increases as a linear function of radius. It is worth noting that the magnetic field has no effect on the electrons positioned on the axis of the DLW at any given phase.

B. Phase velocity and attenuation coefficient

After determining the complex propagation constant k_z , the phase velocity, group velocity, and attenuation coefficient can be derived from Eqs. (17-19).

$$v_{ph} = \frac{\omega}{\beta} \quad (17)$$

$$v_g = \frac{\partial\omega}{\partial\beta} \quad (18)$$

$$\beta = \text{Re}\{k_z\}, \alpha = -\text{Im}\{k_z\} \quad (19)$$

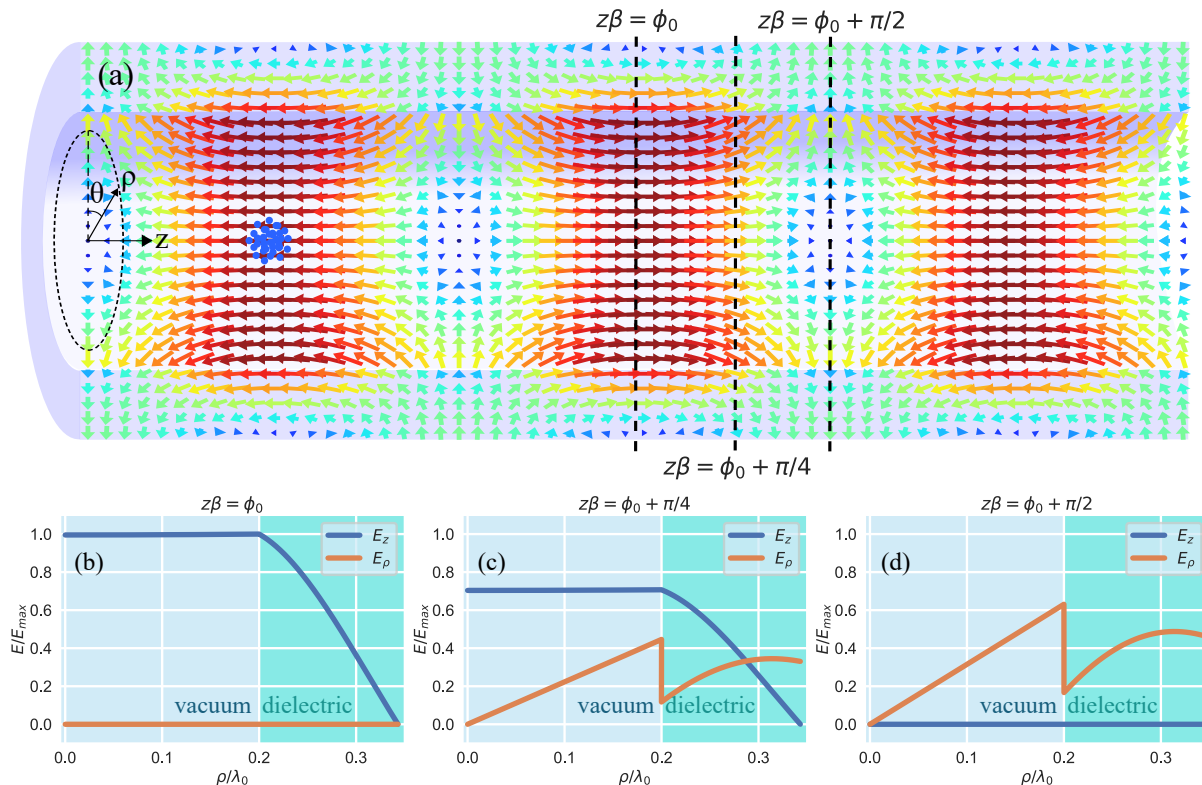


FIG. 4. (a) Electric field distribution of the TM_{01} -mode within the DLW with parameters listed in Table I for a cross section along the waveguide at a fixed time t . The field distribution is radially symmetric around the propagation axis. (b-d) shows the fields over the waveguide cross-section at the different propagation phases indicated in Figure (a). The dielectric thickness-to-vacuum radius ratio has been deliberately selected to align the phase velocity with the speed of light (listed in Table I).

Fig. 5 illustrates normalized phase velocity (normalization with respect to vacuum speed of light), and attenuation coefficient of the TM_{01} -mode of the DLW with a dielectric material having a refractive index of $n_2 = 1.95$ (fused Silica) and absorption coefficient of 10 (Np/m) at 300 GHz [41–46], corresponding to $\epsilon_{r_2} = 3.8 + j0.0016$, which is surrounded by a copper layer with a conductivity of $\sigma = 5.9e7$ (S/m), corresponding to $\epsilon_{r_3} = 1 + j3.6e6$ at the same frequency. Since the refractive index of the dielectric (fused silica) is roughly uniform for a wide range of frequencies below 500 GHz, the calculated phase velocity values are expandable to other frequencies. But since the attenuation coefficient varies by frequency, the results for the attenuation are valid only for 300 GHz.

The dimensions of the DLW should be carefully chosen to ensure that the phase velocity is in a range greater than the initial velocity of electrons and less than the vacuum speed of light. To maintain a specific phase velocity, reducing the vacuum radius will necessitate increasing the dielectric thickness (contours of Fig. 5(a)), resulting in changes to the electric field along the axis. In the subsequent section, we will conduct calculations to determine the electric field for different dimensions.

C. Power, field, and group velocity

To determine the electric field over a cross section for a given drive power, we need to compute the total power transported by the TM_{01} -mode of the DLW in terms of the field amplitude. It should be noted that in this paper, we do not yet investigate the coupling to the DLW. Therefore, the terms “power” and “energy” refer to the power and energy transported by the TM_{01} -mode.

In order to calculate the average power (for a sinusoidally varying field) through an area s with unit normal vector \hat{n} , one needs to compute the time-averaged integral of the inner product of the Poynting vector \vec{S} and the normal vector \hat{n} over the cross-sectional area.

$$P_s = \frac{1}{2} \text{Re} \left\{ \iint_s \vec{S} \cdot \hat{n} ds \right\} \quad (20)$$

where \vec{S} is defined by Eq. (21) for complex electric and magnetic fields \vec{E} and \vec{H} .

$$\vec{S} = \frac{1}{2} \vec{E} \times \vec{H}^* \quad (21)$$

Consequently, the total longitudinal power P_z flowing through a cross section of the DLW is computed by integrating the z -component of the Poynting vector S_z over

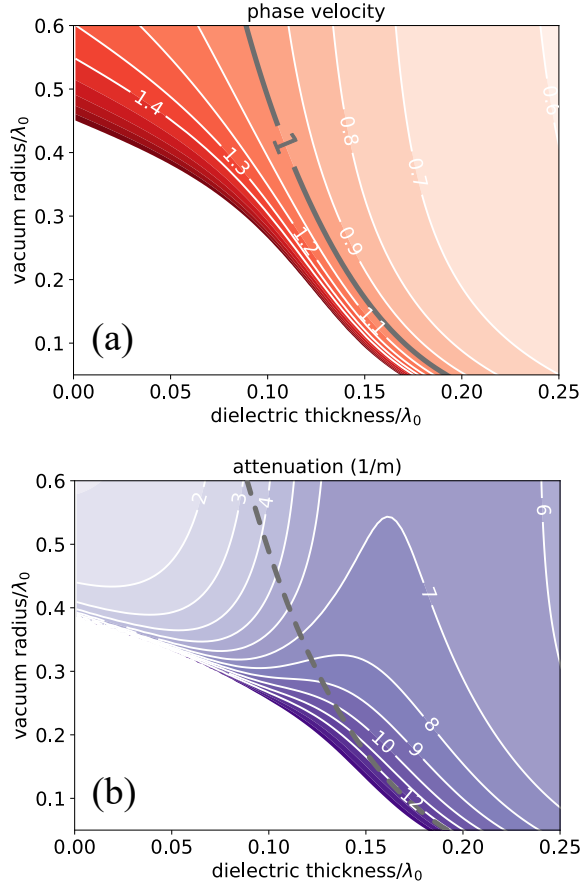


FIG. 5. (a) Phase velocity normalized to the vacuum speed of light, and (b) negative imaginary part of propagation constant, $\alpha = -\text{Im}\{k_z\}$, i.e. attenuation coefficient, of the TM_{01} -mode of the DLW versus vacuum radius and dielectric thickness normalized to vacuum wavelength (since the phase velocity is independent of wavelength for a given complex refractive indices of the dielectric ϵ_2 and metal ϵ_3). Here we assumed $\epsilon_{r2} = 3.8 + j0.0016$ and $\sigma_3 = 5.96e7 \text{ S/m}$ at 300GHz.

$$P_z = P_{z1} + P_{z2} + P_{z3} = \int_0^{\rho_1} \int_0^{2\pi} S_z(A_1) \rho d\theta d\rho + \int_{\rho_1}^{\rho_2} \int_0^{2\pi} S_z(A_2, B_2) \rho d\theta d\rho + \int_{\rho_2}^{\infty} \int_0^{2\pi} S_z(A_3) \rho d\theta d\rho \quad (22)$$

The coefficients A_2 , B_2 , and A_3 could be written as functions of A_1 utilizing Eq. (15). By equating the right side of Eq. (22) to the given power, it becomes possible to calculate the coefficients A_1 , A_2 , B_2 , A_3 and consequently, determine the absolute value of the electromagnetic field within the DLW where the axial electric field E_z is the primary field component responsible for acceleration. Fig. 6 illustrates the axial electric field of the cylindrical DLW for a unit power of 1 W.

Considering that the power flow in the layers has been computed to determine the absolute field values, we can employ a simpler method than Eq. (18) to calculate the

the entire cross-sectional area. For the given three-layer structure, the relationship can be expressed by Eq. (22).

group velocity. The connection between group and phase velocity, as revealed through axial power flow within the structure, is examined in [47]. The relationship between v_{ph} and v_g relative to c (vacuum speed of light) can be described as

$$\frac{v_{ph}v_g}{c^2} = \frac{\int_s S_z ds}{\int_s n^2 S_z ds} \quad (23)$$

Here, s represents the entire cross-section of the waveguide. We have calculated phase velocity v_{ph} , power flow in the vacuum layer P_{z1} , and power flow in the dielectric layer P_{z2} by Eq. (22). Consequently, the normalized

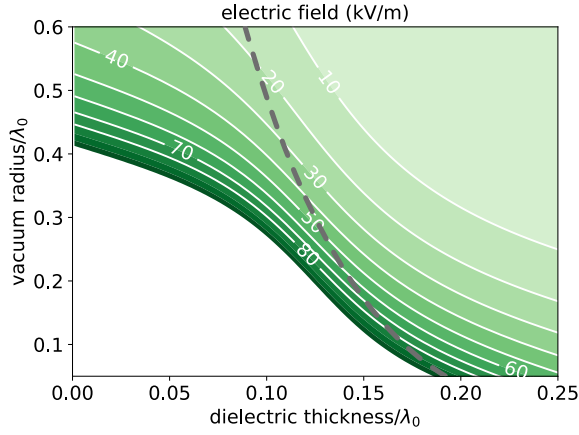


FIG. 6. Longitudinal component of the electric field on the axis of the DLW considering a unit power of 1W for the parameters listed in Table I. The gray dashed line indicates the condition for phase velocity equal to the speed of light.

group velocity can be expressed as

$$\frac{v_g}{c} = \frac{c (P_{z1} + P_{z2})}{v_{ph} (P_{z1} + \epsilon_2 P_{z2})} \quad (24)$$

We note that the power flow through metal P_{z3} is neglected. Fig. 7 shows the normalized group velocity of the TM_{01} -mode. As can be derived from Eq. (24), an increase in the power flow through the dielectric region leads to a reduction in group velocity. The minimum group velocity of the TM_{01} -mode (for normalized phase velocity of 1) is $\frac{1}{\epsilon_2}$, which is approached for very small vacuum radii. As depicted in Fig. 7, the group velocity

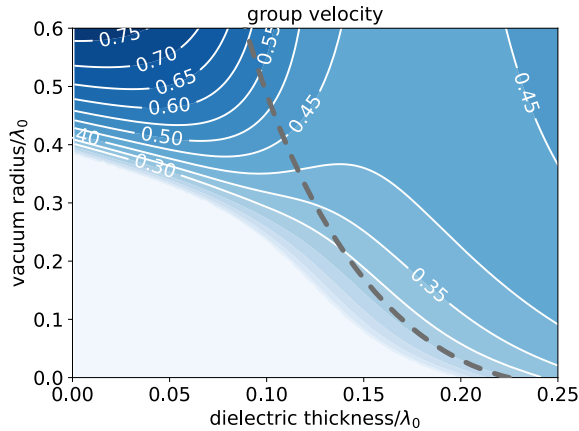


FIG. 7. Group velocity of the TM_{01} -mode normalized to the vacuum speed of light for the parameters listed in Table I. The gray dashed line indicates the condition for phase velocity equal to the speed of light.

is much lower than the speed of light. Evidently, achieving larger group velocity values is desirable as it allows the electron to interact with the THz pulse over a longer

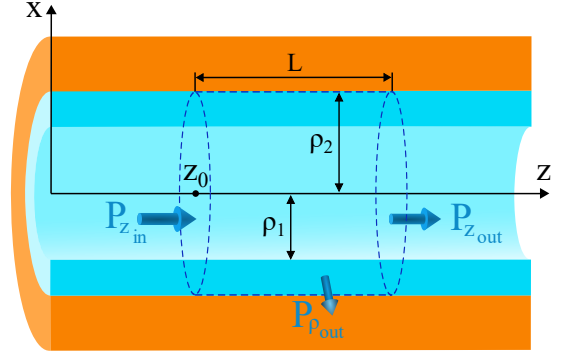


FIG. 8. Power flows for a cylinder with the radius of ρ_2 . $P_{\rho_{out}}$ is the outward radial power flow over a length L . $P_{z_{in}}$ and $P_{z_{out}}$ are longitudinal powers flowing into and out of the cylinder.

distance. However, obtaining higher group velocities necessitates increasing the vacuum radius, which, in turn, leads to a reduced accelerating field for a given power. A previous study introduced an upper limit for the group velocity based on the axial and transverse electric field strengths at the edges of the vacuum region [48].

$$v_g \leq \frac{c}{1 + 2 \left(\frac{E_z}{|\mathbf{E}_{\perp}|} \right)^2} \quad (25)$$

where \mathbf{E}_{\perp} represents the transverse electric field, equivalent to E_{ρ} for the TM_{01} -mode. As evident from Eq. (25), increasing the group velocity will result in a reduced accelerating field E_z .

Up to this point, we have employed the Poynting vector to determine the accelerating field and group velocity. Now, we want to utilize it to calculate the power attenuation within both the dielectric and metallic layers. The attenuation values calculated in the preceding section accounted for losses in the entire structure, including both dielectric and metal losses. To determine the individual contribution of each layer to the overall attenuation, one could integrate the dissipated power over the volume. We choose to calculate the dissipated power within the dielectric layer using the Poynting theorem. We consider a cylinder with radius ρ_2 as depicted in Fig. 8, where the term $P_{\rho_{out}}$ denotes the radial power flow through the dielectric-metal interface over a length L . $P_{z_{in}}$ and $P_{z_{out}}$ refer to the axial power flow entering and exiting the cylinder, respectively.

The conservation relation for the power flows and dissipated power within the cylinder in Fig. 8 can be expressed as

$$P_{z_{in}}(\rho) = P_{\rho_{out}}(\rho) + P_{z_{out}}(\rho) + P_{d_{dielectric}} \quad (26)$$

where $P_{d_{dielectric}}$ is the dissipated power within the dielectric layer. By utilizing Eqs. (14), (20), and (21) the output power flow $P_{z_{out}}$ can be expressed as $e^{-2\alpha L} P_{z_{in}}$ since all the fields are attenuated with the attenuation

constant α . Thus, the dissipated power within the di-

electric is calculated as

$$\begin{aligned}
 P_{d_{\text{dielectric}}} &= (1 - e^{-2\alpha L}) P_{z_{\text{in}}} - \int_{z_0}^{z_0+L} \int_0^{2\pi} \frac{1}{2} \text{Re} \left\{ E_z(\rho_2, z_0) H_\phi^*(\rho_2, z_0) e^{-2\alpha(z-z_0)} \rho_2 d\theta dz \right\} \\
 &= (1 - e^{-2\alpha L}) \left(P_{z_{\text{in}}} - \frac{\pi \rho \text{Re} \left\{ E_z(\rho_2, z_0) H_\phi^*(\rho_2, z_0) \right\}}{2\alpha} \right)
 \end{aligned} \tag{27}$$

Notably, due to axial symmetry of the electric and magnetic fields for the TM_{01} -mode, the angular integration term, is replaced by 2π . The total power loss $P_{d_{\text{total}}}$ could be formulated using the same method assuming a cylinder with a sufficiently large diameter. If the skin depth of the metallic layer is very short in comparison with the dimension of the DLW, the longitudinal power flow within the metallic layer is accordingly negligible in comparison with the power flow inside the dielectric and vacuum ($P_{z_3} \ll P_{z_1} + P_{z_2}$). Consequently, the total dissipated power can be written as

$$P_{d_{\text{total}}} \cong P_{z_{\text{out}}} - P_{z_{\text{in}}} = (1 - e^{-2\alpha L}) P_{z_{\text{in}}} \tag{28}$$

$P_{z_{\text{in}}}$ is determined by integrating the z-component of the Poynting vector over the flat surface of the cylinder (Fig. 8) as utilized for calculating the power flow in Eq. (22). Therefore $P_{d_{\text{total}}}$ is

$$P_{d_{\text{total}}} \cong (1 - e^{-2\alpha L}) \pi \int_0^{\rho_2} \text{Re} \left\{ E_\rho(\rho) H_\phi^*(\rho) \right\} \rho d\rho \tag{29}$$

The ratio of the dissipated power inside the metallic and dielectric layers to the total dissipated power could be formulated as

$$\frac{P_{d_{\text{dielectric}}}}{P_{d_{\text{total}}}} \cong 1 - \frac{\rho_2 \text{Re} \left\{ E_z(\rho_2, z_0) H_\phi^*(\rho_2, z_0) \right\}}{2\alpha \int_0^{\rho_2} \text{Re} \left\{ E_\rho(\rho) H_\phi^*(\rho) \right\} \rho d\rho} \tag{30a}$$

$$\frac{P_{d_{\text{metal}}}}{P_{d_{\text{total}}}} \cong \frac{\rho_2 \text{Re} \left\{ E_z(\rho_2, z_0) H_\phi^*(\rho_2, z_0) \right\}}{2\alpha \int_0^{\rho_2} \text{Re} \left\{ E_\rho(\rho) H_\phi^*(\rho) \right\} \rho d\rho} \tag{30b}$$

In order to see the effect of the metal loss on the dissipated power, different materials are examined. Table II shows the conductivity of some metals and its approximate equivalent skin depth at 300 GHz (skin depths are calculated with low frequency conductivity values [49–51]). Although, the conductivity values are valid for a wide range of frequencies from DC to THz, one can employ the classical Drude model for more precise calculations [52, 53].

Table III presents the total attenuation coefficient α for the TM_{01} -mode of the DLW and relative dissipated power within each layer for various metals and three different vacuum radii at the frequency of 300 GHz. The

TABLE II. Conductivity and skin depth for various metals at 300 GHz

Material	Conductivity (S/m)	Skin depth (nm)
Silver	6.2×10^7	~ 116
Copper	5.9×10^7	~ 119
Gold	4.5×10^7	~ 137
Chromium	7.9×10^6	~ 326
Titanium	2.5×10^6	~ 580

dielectric layer is composed of fused silica with the refractive index of 1.95 and attenuation coefficient 10 Np/m at 300 GHz [45]. The dielectric thickness is optimized for each vacuum radius to set the phase velocity to the speed of light.

As evident from the values in Table III, the fractional attenuation in the dielectric remains relatively consistent irrespective of the metal. Altering the vacuum radius while keeping the phase velocity constant (at the speed of light) has a limited effect on the attenuation level. However, it significantly affects the axial electric field due to the substantial changes in cross-sectional area.

To explore the impact of changing the frequency, we present a comparison of the attenuation coefficient of the DLW at three frequencies: 200 GHz, 300 GHz, and 400 GHz in Table IV (at a fixed vacuum radius of 200 μm). The refractive index of the dielectric layer (fused silica) shows little variation within this frequency range, but the attenuation coefficient varies from ~ 6 Np/m at 200 GHz to ~ 18 Np/m at 400 GHz [41–46].

Up to this point, we have explored the electromagnetic properties of the DLW. Our assumption is that the presence of a low-current electron beam does not significantly alter these electromagnetic fields. Neglecting the fields of the particles in the waveguide, i.e. wakefields, the computed field distributions enable us to solve the relativistic equation of motion of charged particles in the DLW. In the following section, our focus will shift towards solving the equation of motion for an individual electron positioned on the axis of the DLW and determining its acceleration.

TABLE III. Dielectric attenuation and metal attenuation comparison for various vacuum radii

Vacuum radius	Total Attenuation (m^{-1})			Dielectric Attenuation to Total Attenuation			Metal Attenuation to Total Attenuation		
	150 μm	200 μm	250 μm	150 μm	200 μm	250 μm	150 μm	200 μm	250 μm
Dielectric thickness	154.4 μm	143.1 μm	132.8 μm	154.4 μm	143.1 μm	132.8 μm	154.4 μm	143.1 μm	132.8 μm
Material									
Silver	10.8	9.9	8.8	37 %	35 %	32 %	63 %	65 %	68 %
Copper	11.0	10.1	9.0	37 %	34 %	32 %	63 %	66 %	68 %
Gold	12.0	11.0	9.9	34 %	31 %	29 %	66 %	69 %	71 %
Chromium	23.1	21.7	19.7	18 %	16 %	14 %	82 %	84 %	86 %
Titanium	37.9	35.8	32.7	11 %	10 %	9 %	89 %	90 %	91 %

TABLE IV. Dielectric attenuation and metal attenuation comparison for various frequencies

Frequency	Total Attenuation (m^{-1})			Dielectric Attenuation to Total Attenuation			Metal Attenuation to Total Attenuation		
	200 GHz	300 GHz	400 GHz	200 GHz	300 GHz	400 GHz	200 GHz	300 GHz	400 GHz
Dielectric thickness	238.5 μm	143.1 μm	97.4 μm	238.5 μm	143.1 μm	97.4 μm	238.5 μm	143.1 μm	97.4 μm
Material									
Silver	6.2	9.9	13.6	41 %	35 %	35 %	59 %	65 %	56 %
Copper	6.3	10.1	13.9	40 %	34 %	34 %	60 %	66 %	66 %
Gold	6.9	11.0	15.2	37 %	31 %	31 %	63 %	69 %	69 %
Chromium	12.9	21.7	29.7	20 %	16 %	16 %	80 %	84 %	84 %
Titanium	20.9	35.8	49.0	12 %	10 %	10 %	88 %	90 %	90 %

III. LINEAR ACCELERATION

The DLW LINAC is powered by a multicycle THz pulse traveling down the DLW. In the ideal case, the electron bunch travels together with the negative peak of the electric field. In case of having a nonrelativistic electron bunch, the velocity of the electrons should increase during the acceleration process while the THz pulse maintains a constant phase velocity (a uniform DLW in the acceleration direction assumed). Thus, the relative position of the electron and the THz wave changes as it undergoes acceleration. Consequently, the important aspect to consider is maintaining the electron bunch within a single half-cycle of the THz pulse to prevent deceleration.

The optimal scenario for an individual electron involves setting the phase velocity of the THz pulse higher than the initial velocity of the electron and lower than its final velocity (~ 1). The electron must be initially located in the leading portion of the negative electric field half-cycle in order to maximize the acceleration (optimal initial position is discussed later in this section). At the

beginning, the electron starts to lag behind the front part of the negative half-cycle. However, as the electron accelerates, its velocity gradually approaches and eventually surpasses the phase velocity of the THz pulse. Therefore, it shifts from the lagging position to the leading position in the half-cycle, eventually leaving the accelerating half-cycle and entering the decelerating phase (see Fig. 9). At this time the waveguide or THz field should end (if we are not constrained by a shorter pulse width). Another way to keep the electron in phase right after dephasing is to rephase the electric field using phase shifter structures [54]. Nevertheless, we will continue to focus on the axial uniform DLW. To achieve an optimum design, the THz pulse width should be chosen based on the group velocity to avoid decelerating half-cycles. As the THz pulse propagates, the initially accelerating half-cycle transitions from the forefront rearward to the back end of the pulse due to the lower group velocity in comparison with the phase velocity. The length of the DLW and the pulse width are essential parameters in preventing electron deceleration.

We described the phase slippage of the electron within

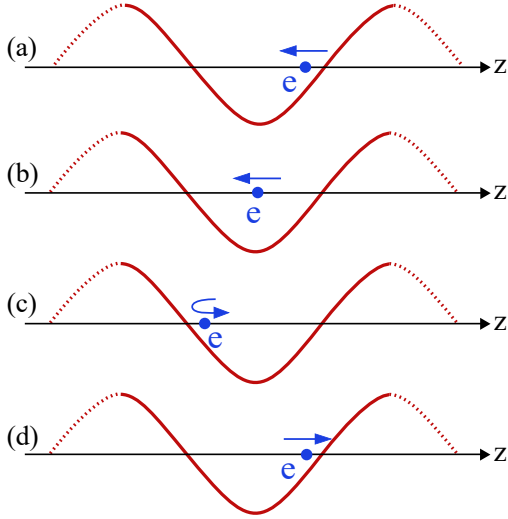


FIG. 9. (a) Electron positioned at the leading part of the negative half-cycle during the initial stage of acceleration with a velocity lower than the phase velocity of the electron. (b) Electron experiencing maximum acceleration. (c) Electron reaching a velocity higher than the phase velocity of the THz pulse and drifting towards the leading part of the half-cycle. (d) Accelerated electron leaving the negative half-cycle and moving into a decelerating, positive half-cycle, which should be avoided. Blue arrows show the velocity of electron relative to the phase velocity of the negative half-cycle.

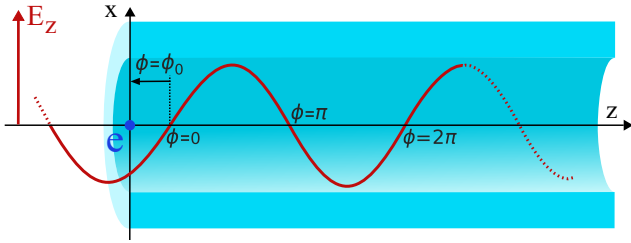


FIG. 10. Relative phase of the electron with respect to the accelerating half-cycle.

the DLW. Now we would like to quantitatively investigate the relative position of the electron with respect to the accelerating half-cycle, and the effect of the injection phase of the electron on the acceleration.

We establish the relative phase of the electron with respect to the accelerating half-cycle as depicted in Fig. 10. Here, we designate ϕ_0 as the relative phase at the moment the electron enters the DLW and call it electron injection phase. Accelerating half-cycles are characterized by phases within the range of $(2p - 1)\pi < \phi < 2p\pi$ while decelerating half-cycles fall within the range of $2p\pi < \phi < (2p + 1)\pi$ (p is an integer number).

Optimal acceleration occurs when we maintain the relative phase of the electron ϕ , between 0 and $-\pi$ (injection phase assumed in the same range). Fig. 11(b) presents the variation in relative phase as the electron

TABLE V. THz pulse parameters

Parameter	Value
THz pulse characteristics	
Frequency	300 GHz
Energy	23 mJ
Duration	467 ps

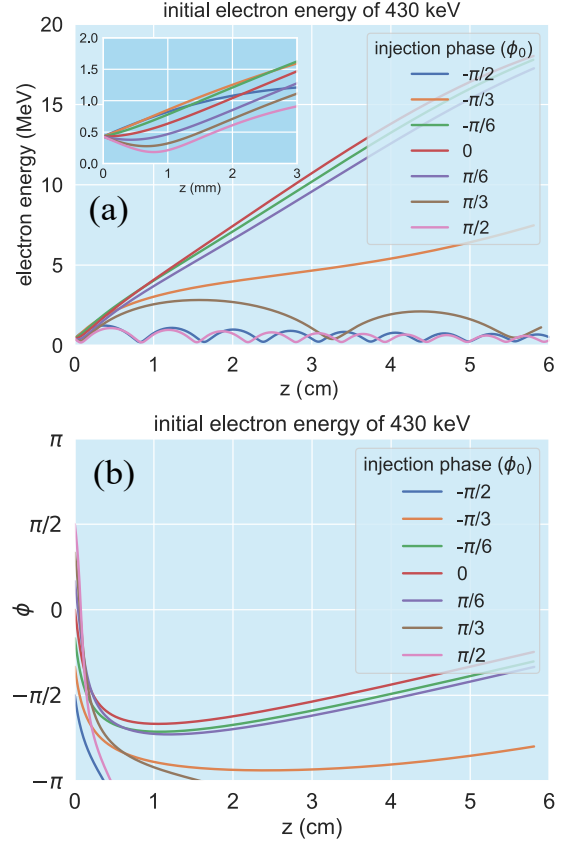


FIG. 11. (a) Kinetic electron energy while being accelerated within the DLW and (b) its relative phase with respect to the accelerating half-cycle for different injection phases.

undergoes acceleration for different injection phase ϕ_0 using the DLW and THz pulse parameters specified in Table I and Table V, respectively.

Fig. 11(b) reveals that electrons injected with phases of $-\frac{\pi}{6}$, 0, $\frac{\pi}{6}$ have experienced notable acceleration compared to their counterparts. Remarkably, the electron injected with a positive phase of $\frac{\pi}{6}$, initially falling within a decelerating half-cycle rapidly transitions to an accelerating half-cycle within the first half of a millimeter of the DLW (as visible in the insets of Fig. 11(a)). Consequently, the final energy of this electron is not significantly lower than that of others.

Fig. 12(a), shows the final kinetic electron energy for different injection phases and initial kinetic electron energy. Increasing the initial kinetic electron energy results in a reduced phase slippage during the acceleration pro-

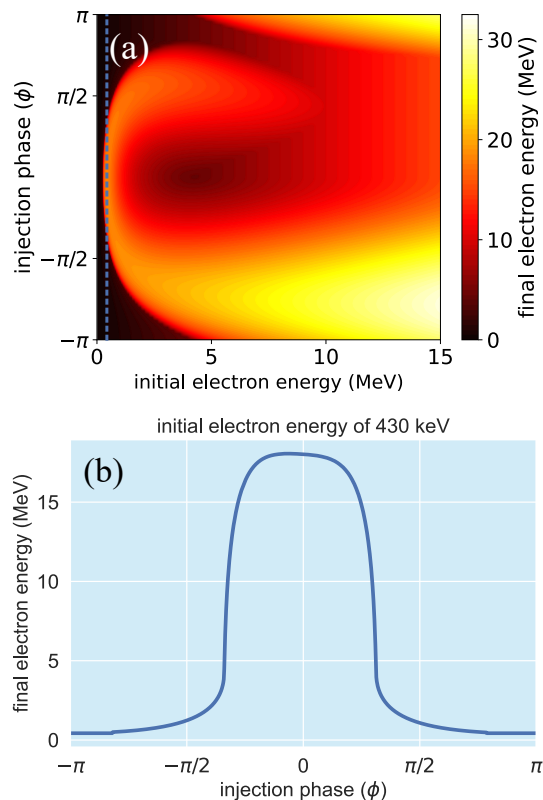


FIG. 12. (a) Final kinetic electron energy for various injection phases and initial kinetic electron energy (b) Final kinetic electron energy on the dashed line in Fig. (a) for a fixed initial electron energy of 430 keV.

cess. This figure underscores the efficiency of injecting high energy electrons close to the peak of the electric field. Notably, for higher electron energy, a similar optimization of the design would be required, including considerations of phase velocity and other relevant factors, but the underlying concept remains the same.

Fig. 12(b) presents the final kinetic electron energy as a function of injection phase, assuming an initial electron energy of 430 keV with the other DLW and THz pulse parameters listed in Table I and Table V.

For this particular design, the optimum injection phase is approximately -14 degrees. Fig. 12 also has relevance for simulating an electron bunch, as electrons within a bunch are injected with varying phases. From Fig. 12(b), it can be deduced that for larger electron bunches (longitudinally expanded), the optimal injection phase will shift towards phases near zero. This aspect will be further investigated in the last section.

IV. DESIGN PARAMETERS

In order to design the DLW and optimize the THz pulse width, we need to fix certain parameters while varying

and optimizing others. In the following subsections, we will explore and identify key parameters.

A. Choice of design parameters

Frequency: In the first section, we found that phase and group velocity calculations can be extended to different frequencies using a scale factor, provided that the DLW is not excessively lossy. However, due to the non-linear nature of the acceleration process, we cannot simply extend the simulation results in the previous sections to different frequencies. Therefore, we will perform the simulations for some frequency range to understand scaling.

Vacuum radius: Determining the optimal vacuum radius presents a challenge. On the one hand, a smaller radius results in a higher electric field inside the DLW (see Fig. 6), but it also leads to a decrease in the acceptable area and electron bunch charge. In addition, the difficulty in fabrication may increase for smaller radii as well as tolerances. Therefore, a compromise must be reached in selecting a vacuum radius that aligns with the designer's and fabrication requirements.

Dielectric refractive index: In this manuscript, we will consider a dielectric refractive index of 1.95 (fused Silica), which remains relatively constant over a wide range of frequencies below 500 GHz [41–46]. It is noted that materials with lower refractive index may require a thicker dielectric to achieve the same phase velocity (lower electric field), while those with higher refractive index may result in a lower group velocity, which is not preferable for a limited duration of the THz pulse. The optimal refractive index may vary depending on the specific parameters.

Metal conductivity: We discussed the power loss within the metal and dielectric layer which is not negligible. Therefore, we will take this loss into account in the simulations, resulting in a decreased final kinetic energy compared to the lossless structure.

B. Varying initial parameters

Initial kinetic electron energy and THz pulse energy: In order to provide guidelines applicable to a wide range of situations, it is necessary to vary specific initial parameters during the design process. This involves considering the impact of the initial kinetic electron energy and THz pulse energy.

C. Parameters to be optimized

The parameters that need to be optimized include the dielectric thickness, electron injection phase, DLW length, and THz pulse width. It is evident that all these parameters are interconnected and should be optimized

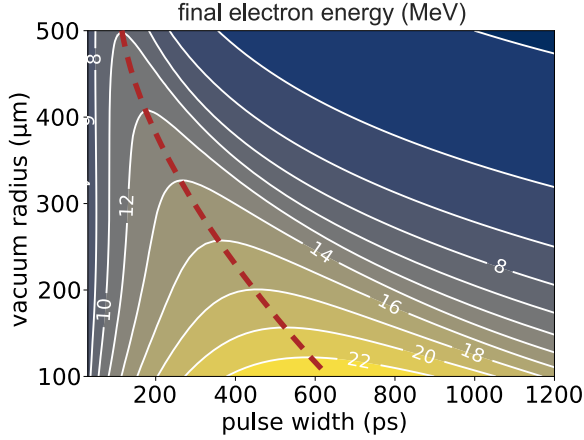


FIG. 13. Maximum achievable kinetic electron energy for various vacuum radii and pulse widths, given a 23 mJ THz pulse and a 430 keV initial kinetic electron energy.

collectively. For the following simulations in this section, we just perform a sensitivity analysis for each parameter around its optimum point to study the impact of each one on the final electron energy. All other parameters have been optimized and are listed in Table VI.

Electron injection phase: As explained in the linear acceleration section, the electron must be injected at the leading part of the negative half-cycle to achieve optimal acceleration. It is crucial to optimize the injection phase of the electron to ensure that it remains within the half cycle for as long as possible, experiencing the maximum acceleration while traveling inside the tube. Thus, the injection phase of the electron is optimized in the following simulations to maximize final kinetic electron energy.

Pulse width: in case of exciting the DLW with a very long THz pulse, the electron falls into the decelerating phase. Conversely, if the THz is too short then the electron outpaces the pulse quickly and cannot be efficiently accelerated. Thus, there exists an optimal pulse width that maximizes acceleration (neglecting DLW dispersion).

Fig. 13 shows the maximum output kinetic energy as a function of vacuum radius and pulse width. Note that the dielectric thickness and the electron injection phase have been optimized for each vacuum radius and pulse width. The other parameters are listed in Table I and Table V.

DLW length: As seen in Fig. 13, there is an optimum pulse width for each vacuum radius to achieve the maximum final electron kinetic energy. The length of the DLW must be chosen in a way that the electrons lead the THz pulse where the DLW ends.

Dielectric thickness: By varying the DLW dimensions for a given dielectric, the phase and group velocity are controlled, and there exist optimum dimensions that yield maximum acceleration.

Fig. 14 illustrates the maximum achievable kinetic energy as a function of the vacuum radius and dielectric

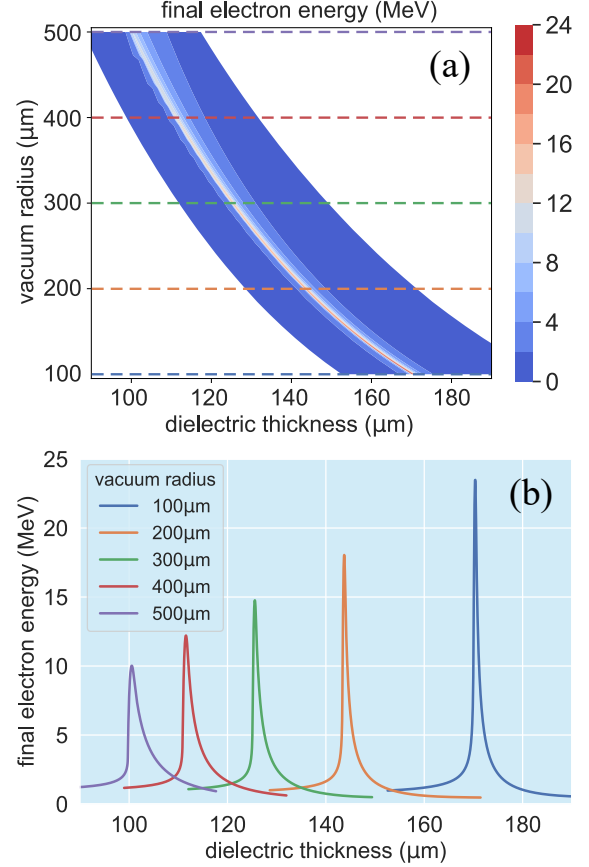


FIG. 14. Maximum achievable electron kinetic energy as a function of vacuum radius and dielectric thickness for parameters listed in Table I and Table V (electron injection phase and THz pulse duration are optimized for each vacuum radius and dielectric thickness).

thickness for parameters listed in Table VI. Note that the THz pulse width has been optimized by considering the results of Fig. 13 for different vacuum radii. The figure shows that reducing the vacuum radius leads to a higher electric field and, subsequently, a higher final electron energy. It's worth noting that there is not an optimum value for the vacuum radius. However, employing a smaller aperture restricts the bunch size and bunch charge. Achieving a balance between these two parameters is beyond the scope of this paper.

Once all the parameters have been optimized, by sweeping the varying parameters, we can generate guideline figures that enable designers to identify the optimum parameters for a cylindrical DLW LINAC. Fig. 15 illustrates the maximum achievable kinetic energy for a single electron on the axis of the DLW for parameters listed in Table VI, considering three different vacuum radii and three different frequencies.

These figures are optimized for a single electron. Therefore, for a bunch of electrons, the average kinetic energy might be slightly lower. Fig. 16 displays the optimal width for the THz pulse. It can be observed that

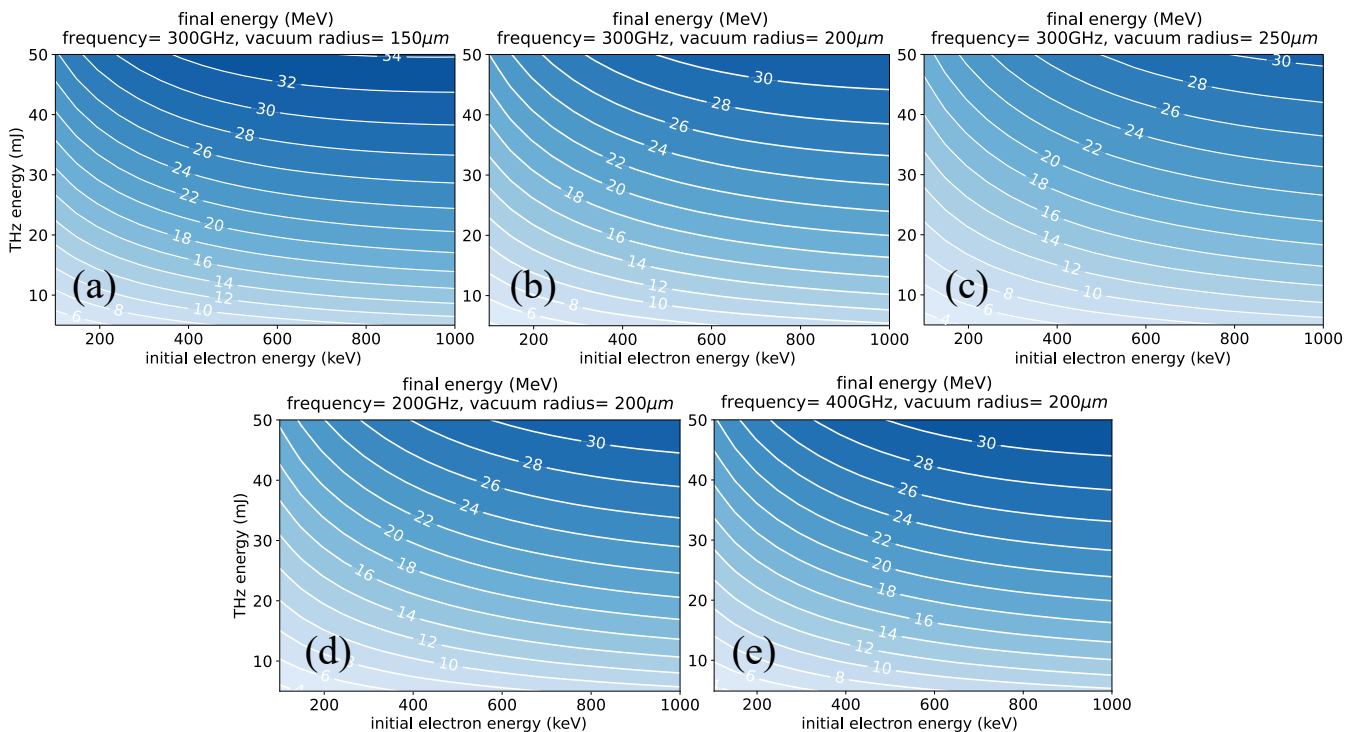


FIG. 15. Maximum achievable kinetic energy for different THz pulse energies and initial kinetic electron energies for different vacuum radii of (a) 150 μ m (b) 200 μ m and (c) 250 μ m at 300 GHz and for (d) 200 GHz and (e) 400 GHz THz pulse for the DLW with a vacuum radius of 200 μ m assuming always optimum injection phase THz pulse width and DLW length, and dielectric thickness.

a higher energy electron and a higher THz pulse energy lead to a longer optimal pulse width. This is because with less phase slippage, electrons can travel further with the accelerating half-cycle.

Fig. 17 shows the optimum DLW length. We can calculate this length based on the optimum pulse width and the group velocity of the THz pulse.

The phase velocity within the DLW can be controlled by adjusting the dielectric thickness. As depicted in Fig. 5(a), varying the dielectric thickness results in significant changes in the phase velocity. Consequently, there exists an optimal thickness for each specific combination of THz energy and electron energy. The corresponding optimum values for the dielectric thickness are presented in Fig. 18.

By utilizing the guideline figures and optimizing the DLW parameters based on initial conditions, designers can customize the DLW LINAC to meet specific requirements. While the simulations presented in this paper are for a single electron on axis of the DLW, it is important to note that the results may vary slightly when simulating an electron bunch. Nevertheless, the designed values obtained from this study serve as a valuable reference and should provide a good starting point for designing and simulating an electron bunch. The optimized parameters offer valuable insights into achieving enhanced performance for THz-driven particle acceleration, making it easier to tailor the DLW LINAC for different scenarios

and applications.

V. BUNCH SIMULATION

Up to this point, our focus has been on simulating and optimizing the DLW and THz pulse parameters for a single electron positioned along the DLW axis. In this section, we shift our attention to simulating an electron bunch on the DLW axis to investigate the longitudinal focusing and defocusing effects of a DLW LINAC. Longitudinal focusing is a critical factor in LINACs, as post-focusing is generally unfeasible. In contrast, transverse focusing can be accomplished using DC fields, such as quadrupole magnets.

When the phase velocity of the THz pulse is set nearly to the speed of light, the longitudinal electric field remains uniform across the aperture, as depicted in Fig. 4. Furthermore, the magnetic fields influence on longitudinal beam parameters is minimal if the radial electron momentum is negligible. Thus, longitudinal focusing is primarily a result of the electric field gradient, making the simulation of a one-dimensional electron bunch on the DLW axis sufficient for studying axial beam parameters.

As depicted in Fig. 4(a), due to the alternating positive and negative electric field gradients along the DLW axis,

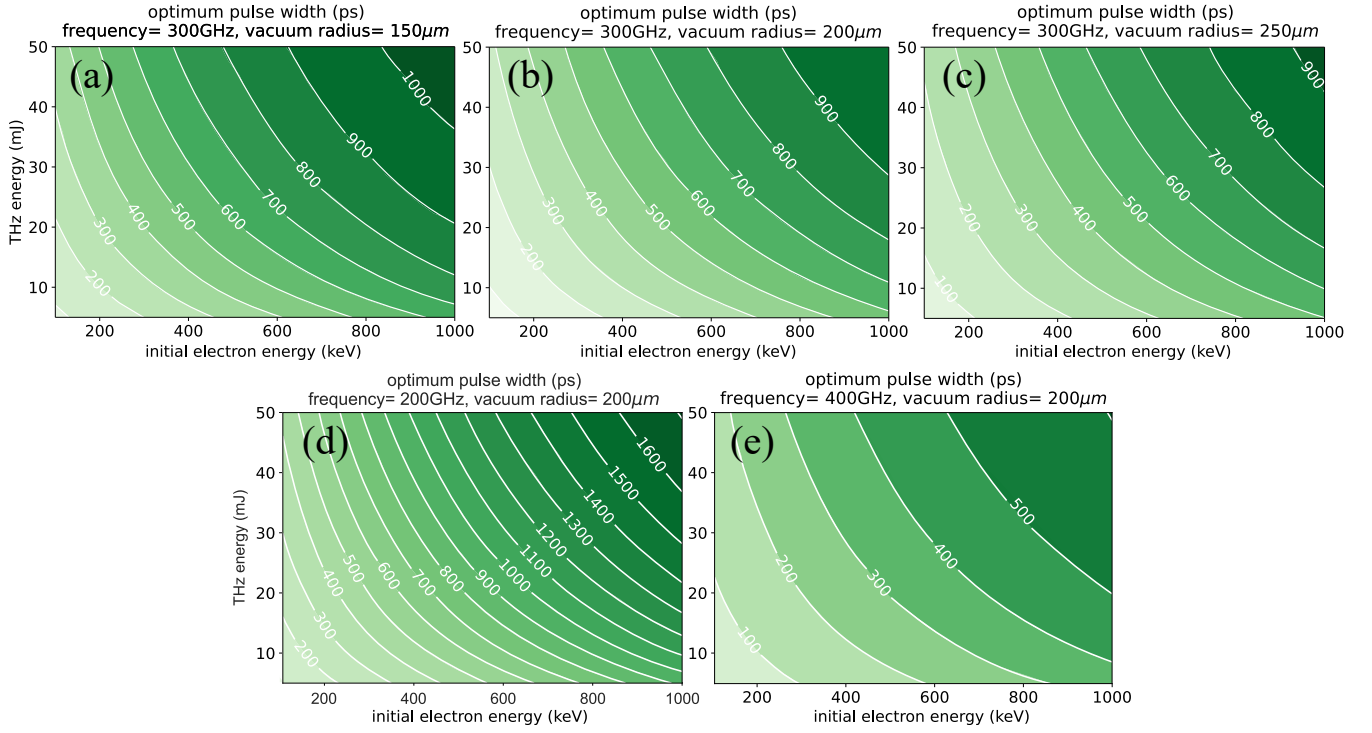


FIG. 16. Optimum THz pulse width for different THz pulse energy and initial kinetic electron energy for different vacuum radii of (a) 150 μm (b) 200 μm and (c) 250 μm at 300 GHz and for (d) 200 GHz and (e) 400 GHz THz pulse for the DLW with a vacuum radius of 200 μm assuming always optimum injection phase and dielectric thickness.

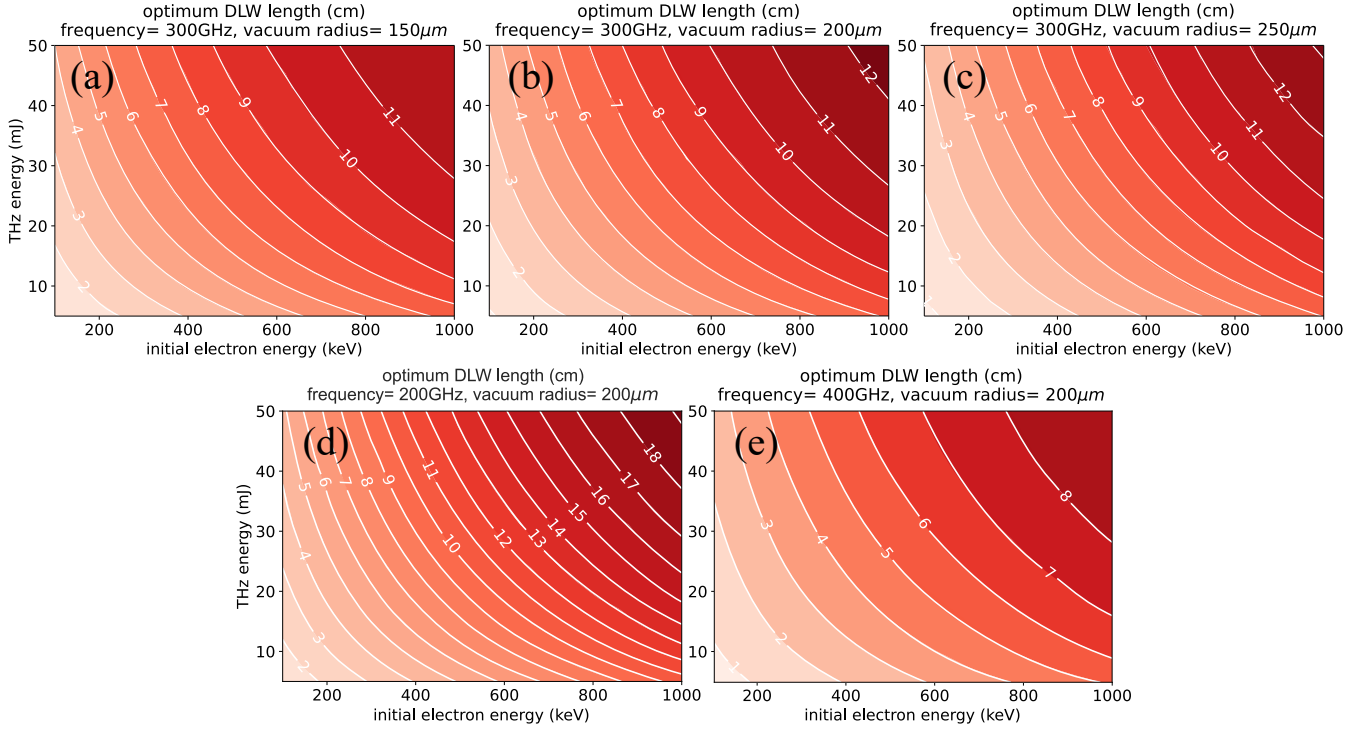


FIG. 17. Optimum DLW length for different THz pulse energy and initial kinetic electron energy for different vacuum radii of (a) 150 μm (b) 200 μm and (c) 250 μm at 300 GHz and for (d) 200 GHz and (e) 400 GHz THz pulse for the DLW with a vacuum radius of 200 μm assuming always optimum injection phase and dielectric thickness.

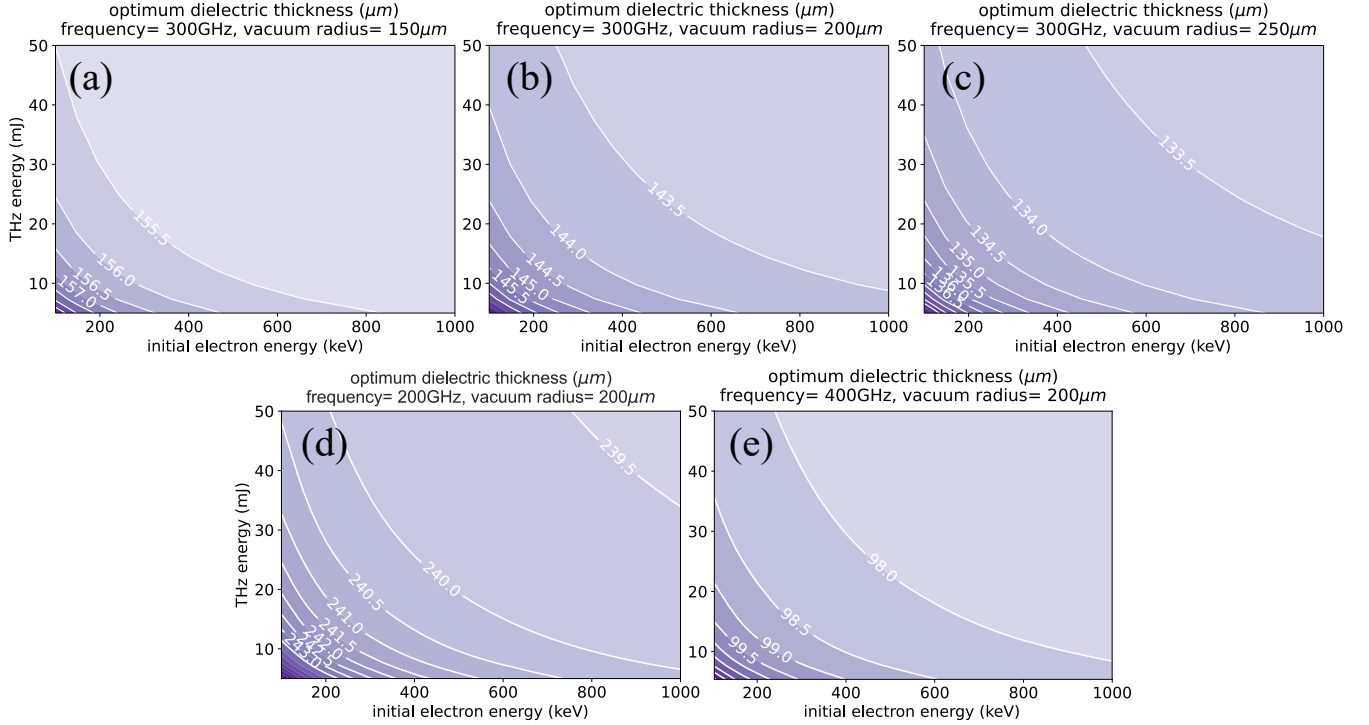


FIG. 18. Optimum dielectric thickness for different THz pulse energy and initial kinetic electron energy for different vacuum radii of (a) 150 μm (b) 200 μm and (c) 250 μm at 300 GHz and for (d) 200 GHz and (e) 400 GHz THz pulse for the DLW with a vacuum radius of 200 μm assuming always optimum injection phase, THz pulse width and DLW length.

electrons within the phase range of $(2p-1)\frac{\pi}{2} < \phi < 2p\frac{\pi}{2}$ experience a focusing field, while those within the range of $2p\frac{\pi}{2} < \phi < (2p+1)\frac{\pi}{2}$ encounter a defocusing field. For a DLW designed for non-relativistic electrons, the phase slippage of electrons relative to the accelerating half-cycle implies that electrons may experience both focusing and defocusing field during acceleration, as shown in Fig. 11(b)).

One method for controlling the axial beam size involves altering the phase velocity of the THz pulse by varying the THz pulse frequency. Deviating from the optimum design will, naturally, reduce the final kinetic energy. However, keeping the electron bunch within the negative or positive field gradient (rather than at the peak field with zero gradient) for a longer duration could be used for manipulating the longitudinal focus point.

For our subsequent simulations, we consider an axial Gaussian distribution for the electron bunch with an rms beam size of 20 μm . Fig. 19 displays the bunch parameters, specifically the longitudinal bunch size as a function of distance, for different frequencies. The DLW and THz pulse parameters are kept the same as detailed in Table I and Table V.

Unlike the injection phase optimization for a single electron explained in Fig. 12(b), for the bunch, we assume a zero-injection phase to maintain all electrons within the accelerating half-cycle.

It is essential to note that since our study primarily

focuses on the electromagnetic fields impact on the electron bunch and the bunch charge is generally quite low (below 1 pC), we disregard the space charge effect in our simulations. All parameters related to the DLW and THz pulse, and the electron bunch are listed in Table VI.

TABLE VI. Parameters of the optimized DLW and THz pulse

Parameter	Value
DLW dimensions	
Vacuum radius	200 μm
Dielectric thickness	143.1 μm
DLW length	5.8 cm
Material properties	
Conductivity of metal	5.96×10^7 S/m
Dielectric refractive index	1.95
Dielectric attenuation constant	
at 200 GHz	6 Np/m
at 300 GHz	10 Np/m
at 400 GHz	18 Np/m
THz pulse characteristics	
THz pulse frequency	300 GHz
THz pulse energy	23 mJ
THz pulse duration	467 ps
Electron bunch characteristics	
Average injection phase	0 degree
Longitudinal rms bunch size	20 μm

Fig. 19 shows the electron bunch parameters during

acceleration for optimized THz pulse and DLW dimension listed in Table VI for different THz pulse frequencies around 300 GHz.

Fig. 19(c) illustrates a substantial reduction in the initial electron beam size, primarily in the DLW's early section, due to the low momentum of the electrons. For the optimal frequency (300 GHz), the output beam is approximately collimated. An increase in frequency results in a reduction of the phase velocity. Consequently, the electron bunch remains in the positive field gradient for a longer duration, leading to beam convergence. This can be inferred from the electron beam energy at the exit of the DLW (Fig. 19(b)) where electrons at the front of the bunch exhibit lower energy and velocity (negative slope). In certain applications, depending on the components downstream of the LINAC, a more tightly converged electron beam may be required. The simulations conducted indicate that achieving this can be accomplished by adjusting the THz frequency. However, it's important to note that such adjustments will result in a reduction in the final energy of the electron beam. It's worth noting that lower frequencies have the potential to maintain the bunch quality due to the gradual slope of the wavelength. Conversely, higher frequencies enable higher field gradients.

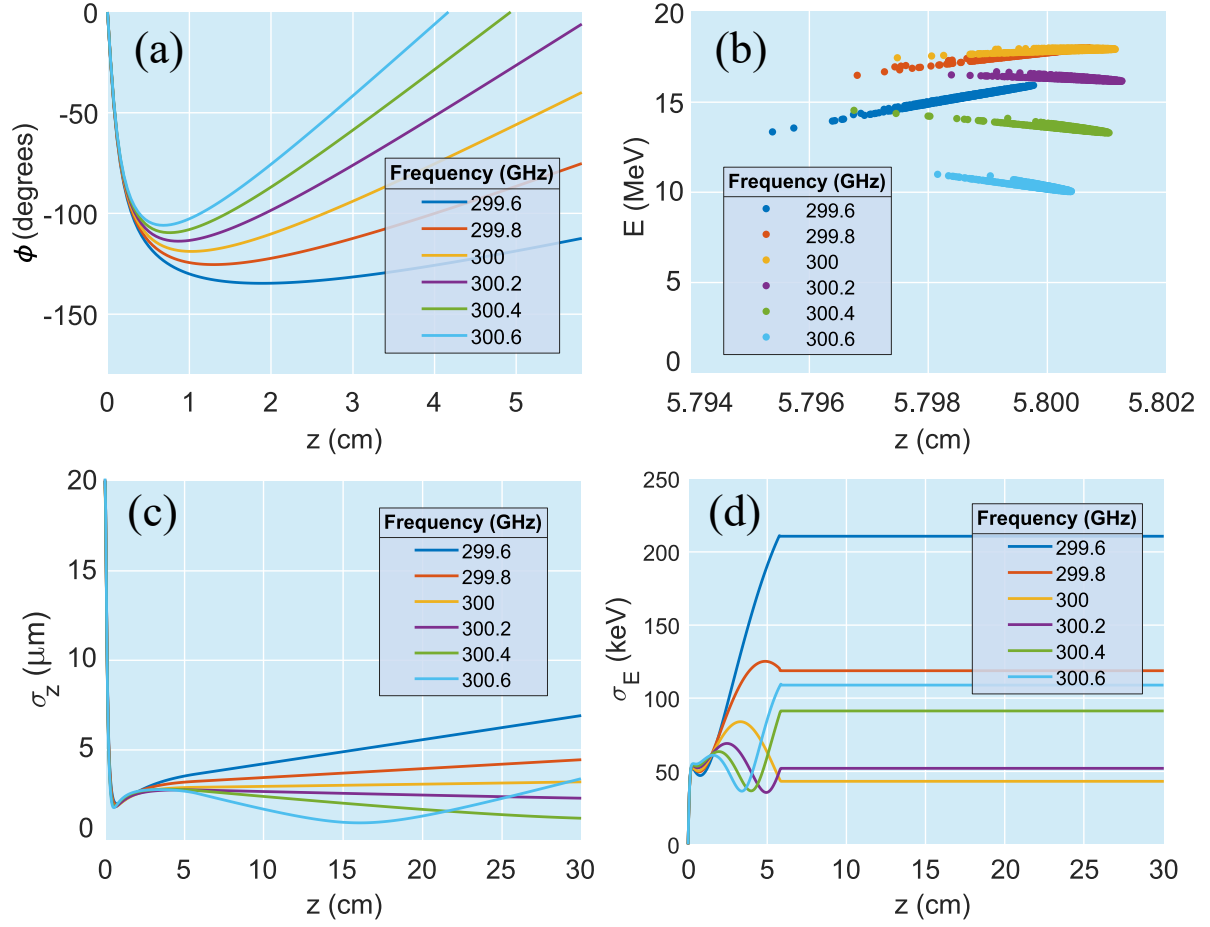


FIG. 19. Electron beam parameters for optimized THz pulse and DLW dimension for different THz pulse frequencies. (a) average phase of the electrons (b) electron bunch energy at the end of the LINAC (c) longitudinal beam size (d) energy spread of the electron beam during acceleration.

VI. CONCLUSION

We presented a comprehensive analytical/numerical guide for optimizing cylindrical dielectric loaded waveguide (DLW) parameters in the context of terahertz (THz) driven linear accelerators (LINACs). By carefully adjusting the dimensions of the dielectric and THz pulse properties, it is possible to control the phase and group velocities within the DLW, and making an effective interaction between the electron and the THz pulse. Thus, optimum electron acceleration can be achieved. The research has identified critical parameters that need to be optimized, such as dielectric thickness, DLW length, THz pulse duration, etc., which play significant roles in maximizing the final kinetic energy of accelerated electrons. What is also remarkable is the relatively weak sensitivity of the resulting electron energy as a function of the frequency used, given a certain THz pulse energy (see Figs. 15-18). The reason is that while, for high THz frequencies, the DLW cross-section becomes smaller, resulting in a higher field at the same intensity and thus allowing for a higher gradient acceleration, the dephasing length and attenuation constant simultaneously becomes shorter and higher. Consequently, the length of the accelerating section pow-

ered is reduced. Therefore, at fixed THz energy, the final electron energy achievable increases only slowly with increasing frequency. The presented guideline figures serve as valuable tools for designers to tailor the accelerator to specific requirements, offering insights into the performance enhancement of THz-driven particle acceleration. Although the simulations are conducted for a single electron on the axis of a DLW and longitudinally spread electron bunches, the obtained optimized values can be considered as a reliable starting point for designing and simulating electron bunches.

ACKNOWLEDGMENTS

The authors acknowledge support by DESY, a Center of the Helmholtz Association, the European Research Council under the European Union's Seventh Framework Programme (FP7/2007-2013) through the Synergy Grant AXISIS (609920), the Cluster of Excellence 'Advanced Imaging of Matter' of the Deutsche Forschungsgemeinschaft (DFG) - EXC 2056 - project ID 390715994 and Project 655350 of the Deutsche Forschungsgemeinschaft (DFG) and the accelerator on a chip program (ACHIP) funded by the Gordon and Betty Moore foundation (GBMF4744).

-
- [1] M. Dal Forno, V. Dolgashev, G. Bowden, C. Clarke, M. Hogan, D. McCormick, A. Novokhatski, B. Spataro, S. Weathersby, and S. G. Tantawi, Rf breakdown tests of mm-wave metallic accelerating structures, *Physical Review Accelerators and Beams* **19**, 011301 (2016).
 - [2] M. Dal Forno, V. Dolgashev, G. Bowden, C. Clarke, M. Hogan, D. McCormick, A. Novokhatski, B. Spataro, S. Weathersby, and S. G. Tantawi, Experimental measurements of rf breakdowns and deflecting gradients in mm-wave metallic accelerating structures, *Physical Review Accelerators and Beams* **19**, 051302 (2016).
 - [3] M. Thompson, H. Badakov, A. Cook, J. Rosenzweig, R. Tikhoplav, G. Travish, I. Blumenfeld, M. Hogan, R. Ischebeck, N. Kirby, *et al.*, Breakdown limits on gigavolt-per-meter electron-beam-driven wakefields in dielectric structures, *Phys. Rev. Lett.* **100**: 214801, 2008 **100** (2008).
 - [4] E. Peralta, K. Soong, R. England, E. Colby, Z. Wu, B. Montazeri, C. McGuinness, J. McNeur, K. Leedle, D. Walz, *et al.*, Demonstration of electron acceleration in a laser-driven dielectric microstructure, *Nature* **503**, 91 (2013).
 - [5] J. Breuer and P. Hommelhoff, Laser-based acceleration of nonrelativistic electrons at a dielectric structure, *Physical review letters* **111**, 134803 (2013).
 - [6] S. Carbajo, E. A. Nanni, L. J. Wong, G. Moriena, P. D. Keathley, G. Laurent, R. D. Miller, and F. X. Kärtner, Direct longitudinal laser acceleration of electrons in free space, *Physical Review Accelerators and Beams* **19**, 021303 (2016).
 - [7] V. Malka, J. Faure, Y. A. Gauduel, E. Lefebvre, A. Rousse, and K. T. Phuoc, Principles and applications of compact laser-plasma accelerators, *Nature physics* **4**, 447 (2008).
 - [8] W. Leemans and E. Esarey, Laser-driven plasma-wave electron accelerators, *Physics today* **62**, 44 (2009).
 - [9] D. Guénot, D. Gustas, A. Vernier, B. Beaupaire, F. Böhle, M. Bocoum, M. Lozano, A. Jullien, R. Lopez-Martens, A. Lifschitz, *et al.*, Relativistic electron beams driven by khz single-cycle light pulses, *Nature Photonics* **11**, 293 (2017).
 - [10] F. Salehi, A. Goers, G. Hine, L. Feder, D. Kuk, B. Miao, D. Woodbury, K.-Y. Kim, and H. Milchberg, MeV electron acceleration at 1 khz with 10 mj laser pulses, *Optics letters* **42**, 215 (2017).
 - [11] Z. He, B. Hou, J. Nees, J. Easter, J. Faure, K. Krushelnick, and A. Thomas, High repetition-rate wakefield electron source generated by few-millijoule, 30 fs laser pulses on a density downramp, *New Journal of Physics* **15**, 053016 (2013).
 - [12] M. Kirchen, S. Jalas, P. Messner, P. Winkler, T. Eichner, L. Hübner, T. Hülsenbusch, L. Jeppe, T. Parikh, M. Schnepf, *et al.*, Optimal beam loading in a laser-plasma accelerator, *Physical review letters* **126**, 174801 (2021).
 - [13] S. Jalas, M. Kirchen, P. Messner, P. Winkler, L. Hübner, J. Dirkwinkel, M. Schnepf, R. Lehe, and A. R. Maier, Bayesian optimization of a laser-plasma accelerator, *Physical review letters* **126**, 104801 (2021).
 - [14] A. Ferran Pousa, I. Agapov, S. Antipov, R. Assmann, R. Brinkmann, S. Jalas, M. Kirchen, W. Leemans,

- A. Maier, A. Martinez de la Ossa, *et al.*, Energy compression and stabilization of laser-plasma accelerators, *Physical Review Letters* **129**, 094801 (2022).
- [15] E. A. Nanni, W. R. Huang, K.-H. Hong, K. Ravi, A. Fallahi, G. Moriena, R. Dwayne Miller, and F. X. Kärtner, Terahertz-driven linear electron acceleration, *Nature communications* **6**, 8486 (2015).
- [16] D. Walsh, D. Lake, E. Snedden, M. Cliffe, D. Graham, and S. Jamison, Demonstration of sub-luminal propagation of single-cycle terahertz pulses for particle acceleration, *Nature communications* **8**, 421 (2017).
- [17] E. Curry, S. Fabbri, J. Maxson, P. Musumeci, and A. Gover, Relativistic electron beam acceleration in a zero-slippage terahertz-driven inverse free electron laser scheme, arXiv preprint arXiv:1708.06385 (2017).
- [18] D. Zhang, A. Fallahi, M. Hemmer, X. Wu, M. Fakhari, Y. Hua, H. Cankaya, A.-L. Calendron, L. E. Zapata, N. H. Matlis, *et al.*, Segmented terahertz electron accelerator and manipulator (steam), *Nature photonics* **12**, 336 (2018).
- [19] L. J. Wong, K.-H. Hong, S. Carbajo, A. Fallahi, P. Piot, M. Soljačić, J. D. Joannopoulos, F. X. Kärtner, and I. Kaminer, Laser-induced linear-field particle acceleration in free space, *Scientific reports* **7**, 11159 (2017).
- [20] G. A. Loew and J. Wang, *RF breakdown studies in room temperature electron linac structures*, Tech. Rep. (Stanford Linear Accelerator Center, Menlo Park, CA (USA), 1988).
- [21] W. Kilpatrick, Criterion for vacuum sparking designed to include both rf and dc, *Review of Scientific Instruments* **28**, 824 (1957).
- [22] S. Dohert, C. Adolphsen, G. Bowden, D. Burke, J. Chan, V. Dolgashev, J. Frisch, K. Jobe, R. Jones, J. Lewandowski, *et al.*, High gradient performance of nlc/glc x-band accelerating structures, in *Proceedings of the 2005 particle accelerator conference* (IEEE, 2005) pp. 372–374.
- [23] X. Wu, D. Kong, S. Hao, Y. Zeng, X. Yu, B. Zhang, M. Dai, S. Liu, J. Wang, Z. Ren, *et al.*, Generation of 13.9-mj terahertz radiation from lithium niobate materials, *Advanced Materials* **35**, 2208947 (2023).
- [24] D. Zhang, A. Fallahi, M. Hemmer, H. Ye, M. Fakhari, Y. Hua, H. Cankaya, A.-L. Calendron, L. E. Zapata, N. H. Matlis, *et al.*, Femtosecond phase control in high-field terahertz-driven ultrafast electron sources, *Optica* **6**, 872 (2019).
- [25] M. A. Othman, J. Picard, S. Schaub, V. A. Dolgashev, S. M. Lewis, J. Neilson, A. Haase, S. Jawla, B. Spataro, R. J. Temkin, *et al.*, Experimental demonstration of externally driven millimeter-wave particle accelerator structure, *Applied Physics Letters* **117** (2020).
- [26] D. Fry, R. R.-S.-HARVIE, L. Mullett, and W. Walkinshaw, Travelling-wave linear accelerator for electrons, *Nature* **160**, 351 (1947).
- [27] V. Ginsburg, Use of the cerenkov effect for the generation of radio waves, in *Dokl. Akad. Nauk*, Vol. 56 (1947) p. 253.
- [28] W. Gai, P. Schoessow, B. Cole, R. Konecny, J. Norem, J. Rosenzweig, and J. Simpson, Experimental demonstration of wake-field effects in dielectric structures, *Physical review letters* **61**, 2756 (1988).
- [29] A. Cook, R. Tikhoplav, S. Tochitsky, G. Travish, O. Williams, and J. Rosenzweig, Observation of narrow-band terahertz coherent cherenkov radiation from a cylindrical dielectric-lined waveguide, *Physical review letters* **103**, 095003 (2009).
- [30] W. Gai, M. Conde, R. Konecny, J. Power, P. Schoessow, X. Sun, and P. Zou, Experimental demonstration of dielectric structure based two beam acceleration, in *AIP Conference Proceedings*, Vol. 569 (American Institute of Physics, 2001) pp. 287–293.
- [31] C. Jing, Dielectric wakefield accelerators, *Reviews of Accelerator Science and Technology* **9**, 127 (2016).
- [32] G. T. Flesher and G. I. Cohn, Dielectric loading for waveguide linear accelerators, *Transactions of the American Institute of Electrical Engineers* **70**, 887 (1951).
- [33] S. Frankel, Tm_{0,1} mode in circular wave guides with two coaxial dielectrics, *Journal of Applied Physics* **18**, 650 (1947).
- [34] M. T. Hibberd, A. L. Healy, D. S. Lake, V. Georgiadis, E. J. Smith, O. J. Finlay, T. H. Pacey, J. K. Jones, Y. Saveliev, D. A. Walsh, *et al.*, Acceleration of relativistic beams using laser-generated terahertz pulses, *Nature Photonics* **14**, 755 (2020).
- [35] D. Zhang, M. Fakhari, H. Cankaya, A.-L. Calendron, N. H. Matlis, and F. X. Kärtner, Cascaded multicycle terahertz-driven ultrafast electron acceleration and manipulation, *Physical Review X* **10**, 011067 (2020).
- [36] H. Xu, L. Yan, Y. Du, W. Huang, Q. Tian, R. Li, Y. Liang, S. Gu, J. Shi, and C. Tang, Cascaded high-gradient terahertz-driven acceleration of relativistic electron beams, *Nature Photonics* **15**, 426 (2021).
- [37] H. Tang, L. Zhao, P. Zhu, X. Zou, J. Qi, Y. Cheng, J. Qiu, X. Hu, W. Song, D. Xiang, *et al.*, Stable and scalable multistage terahertz-driven particle accelerator, *Physical Review Letters* **127**, 074801 (2021).
- [38] X. Yu, Y. Zeng, Y. Bai, L. Song, and Y. Tian, Hollow metal tubes for efficient electron manipulation using terahertz surface waves, *Optics Express* **32**, 3076 (2024).
- [39] X.-Q. Yu, Y.-S. Zeng, L.-W. Song, D.-Y. Kong, S.-B. Hao, J.-Y. Gui, X.-J. Yang, Y. Xu, X.-J. Wu, Y.-X. Leng, *et al.*, Megaelectronvolt electron acceleration driven by terahertz surface waves, *Nature Photonics* **17**, 957 (2023).
- [40] T.-H. E. Fields, *Time harmonic electromagnetic fields* (McGraw-Hill, 1961).
- [41] W. Bagdad and R. Stolen, Far infrared absorption in fused quartz and soft glass, *Journal of Physics and Chemistry of Solids* **29**, 2001 (1968).
- [42] S. Tsuzuki, N. Kuzuu, H. Horikoshi, K. Saito, K. Yamamoto, and M. Tani, Influence of oh-group concentration on optical properties of silica glass in terahertz frequency region, *Applied Physics Express* **8**, 072402 (2015).
- [43] C. Koike, H. Hasegawa, N. Asada, and T. Komatuzaki, Optical constants of fine particles for the infrared region, *Monthly Notices of the Royal Astronomical Society* **239**, 127 (1989).
- [44] M. Naftaly and A. Gregory, Terahertz and microwave optical properties of single-crystal quartz and vitreous silica and the behavior of the boson peak, *Applied Sciences* **11**, 6733 (2021).
- [45] M. N. Afsar and K. J. Button, Millimeter-wave dielectric properties of materials, IN: *Infrared and millimeter waves*. Volume 12 (A85-47960 23-31). Orlando **12**, 1 (1984).
- [46] J. Dutta, C. Jones, and H. Dave, Complex dielectric constants for selected near-millimeter-wave materials at 245 ghz, *IEEE transactions on microwave theory and techniques* **34**, 932 (1986).

- [47] S. Kawakami, Relation between dispersion and power-flow distribution in a dielectric waveguide, *JOSA* **65**, 41 (1975).
- [48] R. J. England, R. J. Noble, K. Bane, D. H. Dowell, C.-K. Ng, J. E. Spencer, S. Tantawi, Z. Wu, R. L. Byer, E. Peralta, *et al.*, Dielectric laser accelerators, *Reviews of Modern Physics* **86**, 1337 (2014).
- [49] R. A. Serway and J. W. Jewett, *Principles of physics*, Vol. 1 (Saunders College Pub. Fort Worth, TX, 1998).
- [50] J. Moore, R. Williams, and D. McElroy, Physical properties of chromium from 77 to 400 k, *Thermal Conductivity* **7**, 297 (1967).
- [51] E. A. Bel'skaya and E. Y. Kulyamina, Electrical resistivity of titanium in the temperature range from 290 to 1800 k, *High Temperature* **45**, 785 (2007).
- [52] S. Liu, J. Hu, Y. Zhang, Z. Zheng, Y. Liu, R. Xu, and Q. Xue, 1 thz micromachined waveguide band-pass filter, *Journal of Infrared, Millimeter, and Terahertz Waves* **37**, 435 (2016).
- [53] N. Smith, Classical generalization of the drude formula for the optical conductivity, *Physical Review B* **64**, 155106 (2001).
- [54] D. Zhang, Y. Zeng, M. Fakhari, X. He, N. H. Matlis, and F. X. Kärtner, Long range terahertz driven electron acceleration using phase shifters, *Applied physics reviews* **9** (2022).